PNAS RESEARCH ARTICLE | CHEMISTRY

The presence and role of the intermediary CO reservoir in heterogeneous electroreduction of CO_2

Sheena Louisia[a,b,1], Dohyung Kim[a,b,c,1], Yifan Li[a,b], Mengyu Gao[c], Sunmoon Yu[b,c], Inwhan Roh[a,b], and Peidong Yang[a,b,c,d,2]

Contributed by Peidong Yang; received February 2, 2022; accepted March 30, 2022; reviewed by Raffaella Buonsanti and Shi Zhang Qiao

Despite the importance of the microenvironment in heterogeneous electrocatalysis, its role remains unclear due to a lack of suitable characterization techniques. Multistep reactions like the electroconversion of CO_2 to multicarbons (C_{2+}) are especially relevant considering the potential creation of a unique microenvironment as part of the reaction pathway. To elucidate the significance of the microenvironment during CO_2 reduction, we develop on-stream substitution of reactant isotope (OSRI), a method that relies on the subsequent introduction of CO_2 isotopes. Combining electrolytic experiments with a numerical model, this method reveals the presence of a reservoir of CO molecules concentrated near the catalyst surface that influences C_{2+} formation. Application of OSRI on a Cu nanoparticle (NP) ensemble and an electropolished Cu foil demonstrates that a CO monolayer covering the surface does not provide the amount of CO intermediates necessary to facilitate C-C coupling. Specifically, the C_{2+} turnover increases only after reaching a density of ~100 CO molecules per surface Cu atom. The Cu NP ensemble satisfies this criterion at an overpotential 100 mV lower than the foil, making it a better candidate for efficient C_{2+} formation. Furthermore, given the same reservoir size, the ensemble's intrinsically higher C-C coupling ability is highlighted by the four-fold higher C_{2+} turnover it achieves at a more positive potential. The OSRI method provides an improved understanding of how the presence of CO intermediates in the microenvironment impacts C_{2+} formation during the electroreduction of CO_2 on Cu surfaces.

heterogeneous catalysis | electrocatalysis | CO_2 reduction | analytical method

Significance

The electroconversion of CO_2 to value-added products is a promising path to sustainable fuels and chemicals. However, the microenvironment that is created during CO_2 electroreduction near the surface of heterogeneous Cu electrocatalysts remains unknown. Its understanding can lead to the development of ways to improve activity and selectivity toward multicarbon products. This work introduces a method called on-stream substitution of reactant isotope that provides quantitative information of the CO intermediate species present on Cu surfaces during electrolysis. An intermediary CO reservoir that contains more CO molecules than typically expected in a surface adsorbed configuration was identified. Its size was shown to be a factor closely associated with the formation of multicarbon products.

Powering the conversion of small molecules into value-added products using renewable electricity is a promising approach to achieve the sustainable production of fuels and chemicals (1–3). The field of electrocatalysis has been moving toward this goal but remains hampered by activity and selectivity challenges. A molecular-level understanding of reactions is required to overcome these difficulties. More importantly, it should involve a thorough consideration of all factors that influence electrochemical conversion at heterogeneous surfaces. Previous studies have suggested that environmental aspects beyond the surface active site may be as critical for facilitating electrocatalytic reactions (4, 5).

Studies in heterogeneous electrocatalysis have largely focused on controlling the active sites and understanding how it influences reaction pathways through techniques such as surface spectroscopy (e.g., in situ Raman and infrared spectroscopy) combined with theory (6–8). However, locally confined environments also play a critical role in mediating reactions as demonstrated in other fields of catalysis. For example, in biocatalysis and homogeneous catalysis, the role of the microenvironment and the secondary coordination sphere have been widely investigated, respectively (9–14). The high selectivity achieved by bio- and molecular catalysts has often been associated with the characteristics of such regimes. Likewise, understanding the influence of a microenvironment in the context of heterogeneous electrocatalysis is necessary to gain a better control of reactions. It is expected that the microenvironment created near a catalytically active surface will exhibit specific physicochemical properties that differ from the bulk.

Microenvironment effects may be especially important for the CO_2 reduction reaction (CO_2RR), particularly on Cu catalysts where a variety of value-added, higher-order products (e.g., ethylene, ethanol) are generated (15). Up to now, probing key surface intermediates using surface spectroscopy coupled with theoretical calculations has led to the consensus that *CO is necessary for the formation of multicarbons (C_{2+}) (16–18). Further investigation has revealed the importance of its binding mode (i.e., $*CO_{atop}$ or $*CO_{bridge}$) in determining CO_2RR selectivity (19–21). Other studies have reported high *CO coverage leading to C-C coupling necessary for C_{2+} formation (22, 23). However, beyond the surface-bound *CO, recent findings suggest the presence of near-surface CO species during CO_2 electroreduction relevant to C_{2+} formation

Author affiliations: [a]Department of Chemistry, University of California, Berkeley, CA 94720; [b]Chemical Sciences Division, Lawrence Berkeley National Laboratory, Berkeley, CA 94720; [c]Department of Materials Science and Engineering, University of California, Berkeley, CA 94720; and [d]Kavli Energy NanoScience Institute, Berkeley, CA 94720

Author contributions: S.L., D.K., and P.Y. designed research; S.L., D.K., Y.L., M.G., S.Y., and I.R. performed research; P.Y. contributed new reagents/analytic tools; S.L., D.K., and P.Y. analyzed data; and S.L., D.K., and P.Y. wrote the paper.

The authors declare no competing interest.

Reviewers: R.B., Ecole Polytechnique Federale de Lausanne; and S.Z.Q., The University of Adelaide, Australia.

[1]S.L. and D.K. contributed equally to this work.

[2]To whom correspondence may be addressed. Email: p_yang@berkeley.edu.

This article contains supporting information online at http://www.pnas.org/lookup/suppl/doi:10.1073/pnas.2201922119/-/DCSupplemental.

Published April 29, 2022.

(24–27). Furthermore, structural modifications presumed to affect the environment surrounding catalysts have been shown to improve C_{2+} selectivity (20, 28–30). Considering its critical influence, an in-depth characterization of the microenvironment under CO_2 electroreduction conditions is needed.

However, the characteristics of the microenvironment remain elusive due to the lack of suitable techniques. Despite the insights acquired into surface species present during the reaction, the use of surface spectroscopy has been limited to analytes present within a few nanometers from the surface (31, 32). Vibrational spectroscopy methods, such as Raman or Fourier-transform infrared spectroscopy, are also constrained to rely on surface enhancing effects to overcome the signal loss associated with the electrolyte (33, 34). Additionally, the enhancement decays rapidly away from the surface (inversely proportional to the cube of the distance), exclusively favoring surface-bound species (35–37). At high catalytic rates, optical interference from product bubble formation limits the use of such techniques under catalytically relevant operando conditions (26, 38). Overall, the limitations of surface vibrational spectroscopy prevent us from understanding the microenvironment during electrochemical reactions on heterogeneous surfaces.

In this work, we introduce on-stream substitution of reactant isotope (OSRI) as a method that can provide insights into the microenvironment near Cu surfaces during CO_2RR. The OSRI method employs isotopic labeling of the reagent CO_2 in a specific sequence and monitors its transformation to various products. Through the analysis of product isotopic compositions, it reveals the presence of a reservoir of intermediary CO (CO_{int}) molecules necessary for C_{2+} formation. Applied to two different systems (i.e., Cu nanoparticle [NP] ensemble and polycrystalline Cu foil), a density reaching ~100 CO_{int} molecules per surface Cu atom is identified as a common characteristic of the reservoir linked to CO_2 conversion to multicarbons. Furthermore, the intrinsic C-C coupling ability of a catalyst can be gauged independently from the availability of CO_{int}. Ultimately, we find that the higher C_{2+} turnover of the Cu NPs compared against the Cu foil originates from both its ability to form a large CO_{int} reservoir at low overpotentials and its intrinsically higher C-C coupling rate. Through the OSRI method, we identify the importance of a CO_{int} reservoir in the formation of C_{2+} over Cu surfaces, which has remained inaccessible thus far from conventional spectroscopic techniques.

Results and Discussion

The OSRI method starts with the application of a cathodic bias under $^{12}CO_{2(g)}$ at a constant flow in aqueous conditions for 1 h, followed by a consecutive hour in which $^{12}CO_{2(g)}$ feed is substituted with $^{13}CO_{2(g)}$ under continued bias (Fig. 1*A*). The propagation of ^{13}C can then be tracked across all products generated during electrolysis, using multiple modes of product analysis in both the gas and liquid phase that quantify the isotopic compositions of different products (Fig. 1*B*). Throughout

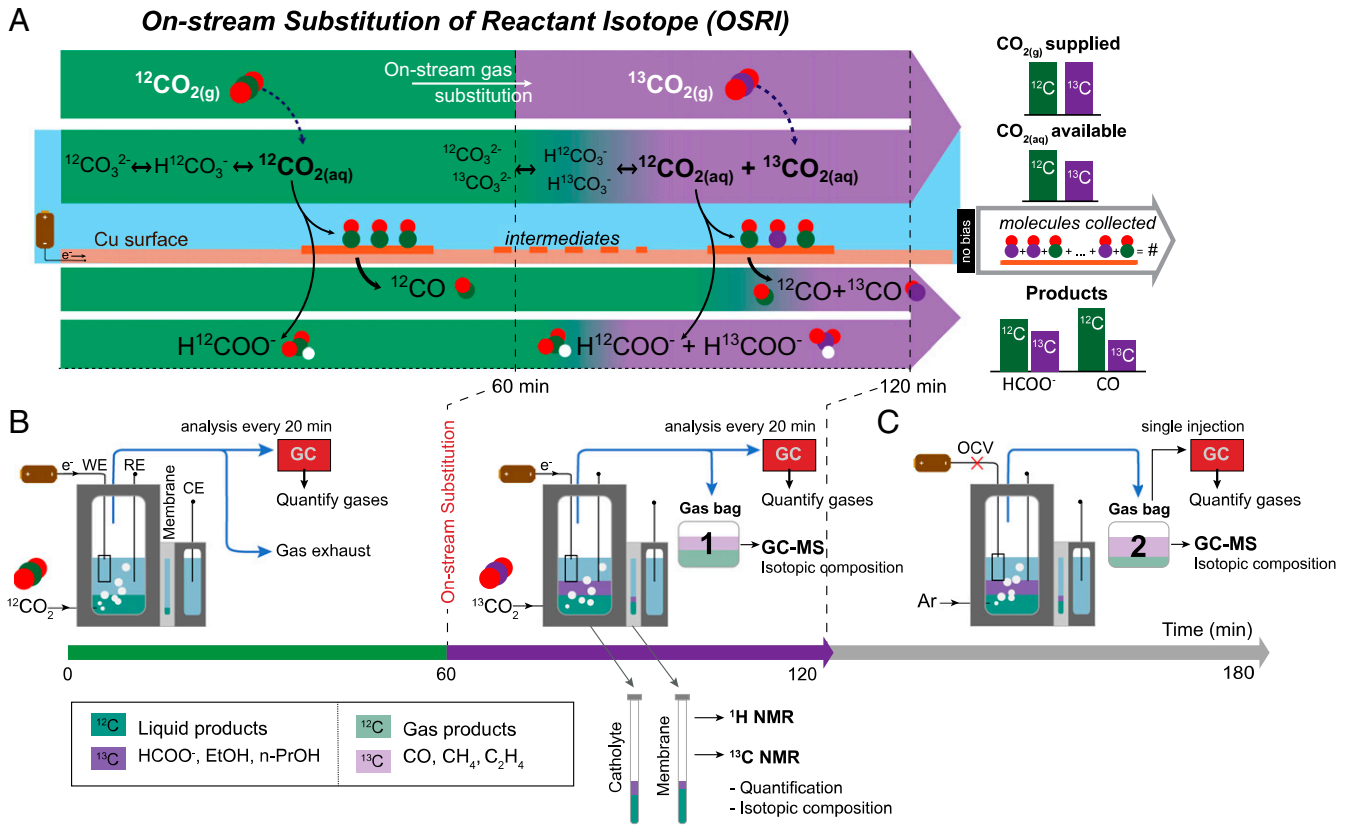

Fig. 1. Study of Cu for CO_2 electroreduction by OSRI. (*A*) Schematic describing OSRI and the catalytic results of Cu. Cathodic bias is applied and maintained for 2 h, while the 0.1 M $KH^{12}CO_3$ electrolyte is purged with $^{12}CO_{2(g)}$ (green) for the first hour followed by $^{13}CO_{2(g)}$ (purple) during the second hour. (*B*) The experimental setup of OSRI where WE, CE, and RE, respectively refer to the working, counter, and reference electrodes. Products that contain ^{12}C (green) and ^{13}C (purple) accumulate in the gas (gas bag #1) and liquid phase (electrolyte) for isotopic analysis by GC-MS and NMR, respectively. All effluent gases are collected in gas bag #1 for the second hour only. Regular quantification of gas products is conducted by sampling the outlet stream at 20-min intervals by GC. NMR spectroscopy is used to quantify and determine the isotopic composition of the liquid products accumulated after 2 h in both the catholyte and the anionic membrane. Formate is the only product that accumulates in the membrane during OSRI. (*C*) After 2 h of electrolysis, the application of bias is terminated (left at open circuit voltage [OCV]), and the electrolyte is purged with Ar into a second gas bag (gas bag #2) for another hour to collect all the gases remaining in the chamber. The contents of gas bag #2 are analyzed using GC (quantification) and GC-MS (isotopic composition).

the 2 h, the outlet gas stream is sampled at regular intervals by gas chromatography (GC) for product quantification in real time. Furthermore, since the products contain a mix of ^{12}C and ^{13}C after switching to $^{13}CO_{2(g)}$, the gas products during the second hour are collected in a gas bag (gas bag #1) to study their isotopic composition by GC-mass spectrometry (GC-MS) (*SI Appendix*, Fig. S1 and Supplementary Text 1). Finally, the liquid products accumulated in the catholyte, as well as the membrane during OSRI, are analyzed using ^{1}H and ^{13}C NMR (*SI Appendix*, Supplementary Texts 2 and 3). Consequently, both the production rate and the isotopic composition of all formed products can be determined (*Materials and Methods*). Throughout OSRI, the current density and product Faradaic efficiencies (FEs) remained stable (*SI Appendix*, Fig. S9). All potentials are reported on the reversible hydrogen electrode (RHE) scale.

The first catalytic system studied by OSRI was an ensemble of 7-nm Cu NPs as reported in previous studies at −0.60 V with CO and $HCOO^-$ as CO_2RR products (39). Because the complete exchange of ^{13}C for the $^{12}CO_{2(aq)}$ is delayed by its equilibration with $H^{12}CO_3^-{}_{(aq)}$, the overall average of $^{12}CO_{2(aq)}$ available should be >50% (Fig. 1*A*). As expected, while the ^{12}C:^{13}C ratio of $CO_{2(g)}$ supplied was 1:1, all products were found with a consistently higher ^{12}C content (Fig. 2*A*). The delay of $CO_{2(aq)}$ to complete the exchange was theoretically verified through a multiphysics simulation (*Materials and Methods*). Regardless of any $CO_{2(aq)}$ consumption taking place at the electrode due to applied potentials, there remains a substantial amount of $^{12}CO_{2(aq)}$ available in solution after an hour of purging $^{13}CO_{2(g)}$ into a $^{12}CO_{2(g)}$ saturated 0.1 M $KH^{12}CO_3$ electrolyte (*SI Appendix*, Fig. S10). The multiple equilibria following $CO_{2(g)}$ dissolution including $HCO_3^-{}_{(aq)}$ and $CO_3^{2-}{}_{(aq)}$ are responsible for the slow exchange of all ^{12}C in solution (*SI Appendix*, Supplementary Text 4 and Fig. S11). It should be noted that the colored segments for $CO_{2(aq)}$ and the products in Fig. 1*A* are simply divided to qualitatively depict their average composition during OSRI; however, the true isotopic shift from ^{12}C to ^{13}C takes place gradually throughout the 2 h as shown in *SI Appendix*, Figs. S10 and S11. Varying the flow rate of $CO_{2(g)}$ or the rate of $CO_{2(aq)}$ consumption results in changes in the isotopic composition of electrolytically available $CO_{2(aq)}$ that are consistent with this analysis (*SI Appendix*, Supplementary Text 5 and Fig. S12).

Although both CO and $HCOO^-$ are enriched in ^{12}C due to the electrolyte equilibration, CO is more enriched in ^{12}C than $HCOO^-$ (Fig. 2*A*). The difference in isotopic composition likely originates from the CO_2-to-$HCOO^-$ mechanism that, unlike the CO_2-to-CO conversion, is known for not involving CO as an intermediate (e.g., *CO) (40–42). Without an accumulation of intermediates involved in $HCOO^-$ formation, its isotopic composition should closely track that of $CO_{2(aq)}$ available during OSRI. On the other hand, a buildup of CO population on a Cu surface is expected for CO formation (40, 43, 44). In previous works, this buildup of CO has been suggested to result in a locally concentrated near-surface CO acting as an intermediate state for CO and, eventually, other higher-order product formation (e.g., C_2H_4) (24, 25, 27). This hypothesis has inspired improved CO_2 reduction strategies by combining CO-generating catalysts (e.g., Ag, Au) with Cu-based electrodes (45–48). Furthermore, these studies infer that chemically adsorbed CO (i.e., *CO) may not be the only configuration of

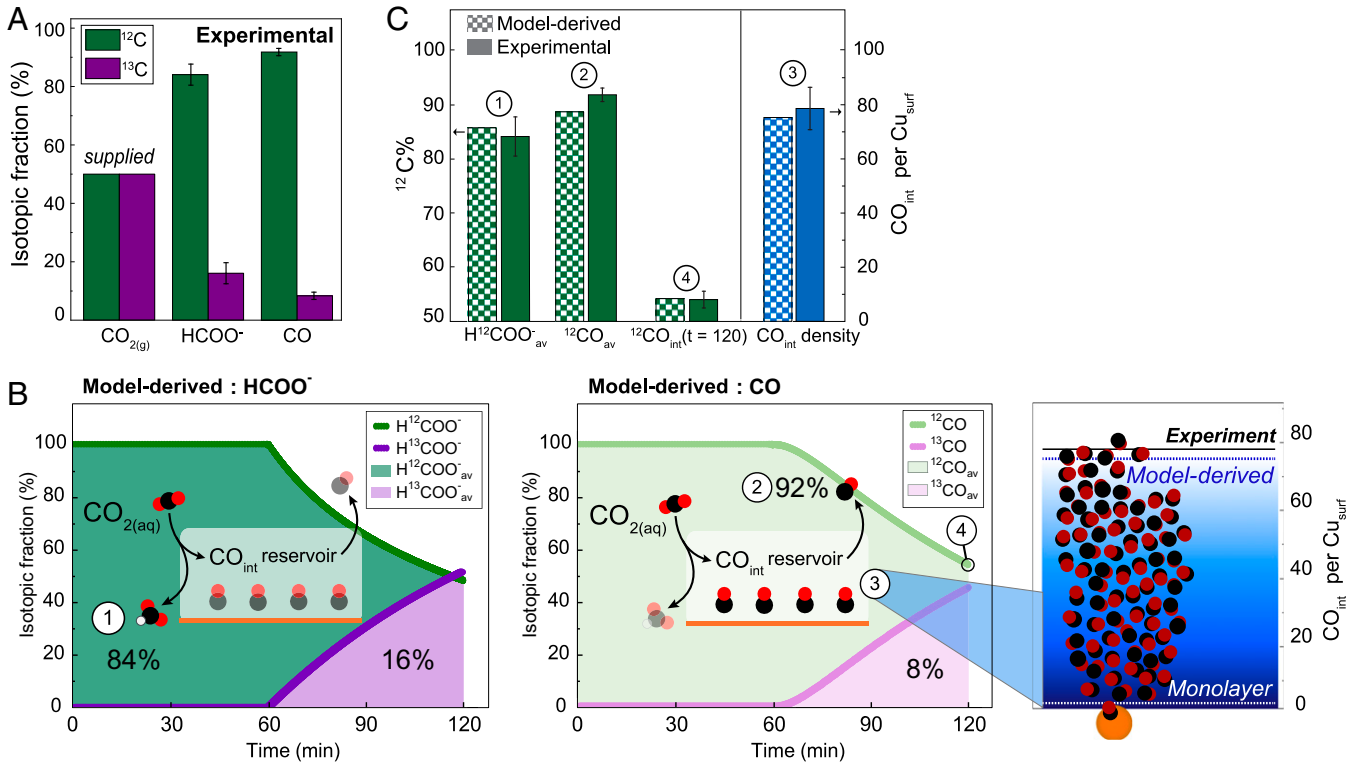

Fig. 2. Identification of the CO_{int} reservoir on the Cu NP ensemble. (*A*) Isotopic composition of $CO_{2(g)}$ supplied and the products of CO_2RR measured during OSRI at −0.6 V vs. RHE. (*B*) Model-derived isotopic composition of $HCOO^-$ and CO produced over time during OSRI considering the presence of a CO_{int} reservoir of constant size at steady state. The green areas under the $H^{12}COO^-$ (dark green) and ^{12}CO (light green) curves divided by the total period (2 h) indicate the average isotopic fraction of ① $^{12}HCOO^-$ and ② ^{12}CO, respectively, for the entire run. The ④ $^{12}CO_{int}$ at the end of OSRI correspond to $^{12}CO_{int}$(t = 120 min). The ③ steady-state density of CO_{int} per Cu_{surf} measured experimentally and reproduced by the model are illustrated and compared to the monolayer of adsorbed *CO. The number of Cu_{surf} was estimated by measuring the postelectrolysis ECSA by Pb underpotential deposition. (*C*) Comparison of model-derived and experimental values for the average isotopic fraction of ① $H^{12}COO^-$ and ② ^{12}CO during OSRI, ③ the steady state CO_{int} density, and ④ the isotopic fraction $^{12}CO_{int}$(t = 120 min). Error bars are one SD of three independent measurements for the experimental data.

CO as an intermediate. Therefore, we refer to all CO species during CO_2 electroreduction, whether chemically bound or otherwise physically confined near the catalyst surface, as CO_{int}. The buildup and formation of a large reservoir of CO_{int} will lead to a lag between the available $CO_{2(aq)}$ (reagent) and CO (product) released at steady state. Specifically, in an experiment that switches from one isotope of $CO_{2(aq)}$ (^{12}C) to another (^{13}C), CO produced is expected to be more enriched in ^{12}C than the average isotopic composition of available $CO_{2(aq)}$ (Fig. 1*A*).

To understand this isotopic lag phenomenon quantitatively, we construct a mathematical model that describes a CO_{int} reservoir attached to a Cu surface during OSRI (Fig. 2*B*). The applicability of the model to the experimental observations was evaluated and confirmed based on its close reproduction of four key experimental results: ① the average isotopic fraction of $H^{12}COO^-$, ② the average isotopic fraction of ^{12}CO, ③ the density of the CO_{int} reservoir per surface Cu atom (Cu_{surf}), and ④ the isotopic fraction of $^{12}CO_{int}$ at the CO_{int} reservoir by the end of OSRI (details available in *SI Appendix*, Supplementary Text 6, and Figs. S13 and S14). Owing to the presence of the CO_{int} reservoir, the model reproduced the delayed exchange to ^{13}C in the CO produced, leading to the trends shown in Fig. 2*B* for the isotopic fraction of $H^{12}COO^-$ and ^{12}CO over time. Values ① and ② are essentially the areas of each curve for $H^{12}COO^-$ and ^{12}CO divided by the entire period (i.e., 120 min), respectively. Furthermore, the steady-state ③ size of the CO_{int} reservoir predicted by the model can be compared to the experimental value measured after stopping the bias at the end of the second hour of OSRI. All CO present in the cell then is purged with Ar for 1 h and collected in gas bag #2 (Fig. 1*C*). The amount of CO_{int} present at steady state near the Cu surface is determined after quantifying all the collected CO and subtracting the headspace and bulk electrolyte-dissolved CO contributions (*Materials and Methods* and *SI Appendix*, Fig. S15). The number of Cu_{surf} necessary to determine the CO_{int} density per Cu_{surf} atom can be derived from Pb underpotential deposition (*SI Appendix*, Supplementary Text 7 and Fig. S16). Because of any possible structural changes that may take place as bias is applied, the electrochemically active surface area (ECSA) of the catalyst was determined postelectrolysis (39, 49). The model also predicts the trend of the isotopic fraction of $^{12}CO_{int}$ throughout OSRI leading to value ④ at 120 min (*SI Appendix*, Fig. S13*D*). The model-derived isotopic fraction of $^{12}CO_{int}$ at this final time point can be compared to the experimental isotopic fraction, measured as 54% ^{12}CO, for all CO remaining postelectrolysis and collected in gas bag #2 (Fig. 1*C*). Overall, the model closely reproduced the experimental values as summarized in Fig. 2*C*.

As stated earlier, the difference in isotopic composition between values ① and ② is a result of the CO_{int} reservoir being present during CO_2 electrolysis. Changing experimental conditions to accelerate the rate of $CO_{2(aq)}$ exchange from ^{12}C to ^{13}C (e.g., by the use of a liquid flow cell simultaneously switching to a $KH^{13}CO_3$ electrolyte) does not alter this difference (*SI Appendix*, Fig. S17). The duration of operation upon substituting to $^{13}CO_{2(g)}$ is another parameter that could be considered, and a longer electrolysis period is not desirable as the larger amount of total products formed obscures the relative difference between $H^{12}COO^-$ and ^{12}CO (*SI Appendix*, Fig. S18). Altogether, the chosen experimental conditions that define OSRI are adequate to assess the presence of the CO_{int} reservoir.

The results obtained from OSRI and reproduced by the model confirm the hypothesis of a CO_{int} reservoir present during CO_2RR. Furthermore, the size of the CO_{int} reservoir verified offers valuable insights into the local environment of catalytically active Cu surfaces during CO_2 electrolysis. We find that the CO_{int} density is around 78 CO_{int} per Cu_{surf}, which is much higher than the monolayer coverage expected for *CO alone (i.e., 1 CO_{int} per Cu_{surf}) (Fig. 2*B*). Assuming that this density of CO_{int} molecules is confined in a volume extending as far as ∼100 μm from the electrode (i.e., up to the Nernst diffusion layer), then its concentration is ∼18 mM (where typical CO solubility in water is 1 mM). Such a high concentration (20 to 100 times the solubility) has previously been verified near the surface of gas-evolving electrodes and is associated with gas bubble nucleation and growth (50–54). Although not reported for CO specifically, its physical properties akin to H_2 or N_2 suggest it would behave similarly during electrolysis (*SI Appendix*, Supplementary Text 8 and Table S7). Therefore, we expect the physical state of CO_{int} to approach a condensed gas phase on and near the electrode surface. Such a large accumulation of CO molecules is likely enabled by the physical properties of the electrode-gas-electrolyte interface formed during CO_2 electrolysis. In the presence of a large production of CO molecules, the Cu electrode can facilitate heterogeneous bubble nucleation on its surface by lowering the energy barrier of this process (50–54). We hypothesize that these favorable conditions for bubble formation enable the retention of a high CO_{int} density close to the catalyst surface.

To understand the role of the CO_{int} reservoir in the formation of C_{2+} products, we investigated more negative potentials where a CO_2-to-C_{2+} conversion takes place. Experimentally, not only were the C_{2+} products also higher in ^{12}C content relative to $HCOO^-$ but also they shared a similar average isotopic composition with CO, highly suggesting that the CO_{int} reservoir acts both as a source of product CO and as an intermediate pool for C_{2+} (*SI Appendix*, Fig. S19). The model was therefore expanded to reproduce the isotopic composition of C_{2+} products, as well as $HCOO^-$ and CO, at more negative potentials. The conversion rate of the CO_{int} reservoir was adjusted to include the amount of CO_{int} consumed to C_{2+} products (*SI Appendix*, Supplementary Text 9). Once more, the model was found to closely reproduce the experimental data obtained during OSRI supporting the CO_{int} reservoir as an intermediate to C_{2+} formation. For instance, the isotopic composition of gas products measured in real time by GC-MS for the CO-derived products, such as CO and C_2H_4, matched closely with the trend expected by the model (Fig. 3*A* and *SI Appendix*, Fig. S21). Similarly, the isotopic composition of $HCOO^-$ measured at different time intervals (e.g., 80 and 100 min) by ^1H NMR matched closely with the corresponding $H^{12}COO^-_{av}$ expected by the model (*SI Appendix*, Fig. S22). Furthermore, the model closely replicated all the experimental values ① to ④ (*SI Appendix*, Fig. S20). Overall, instead of the traditional reaction pathway of CO_2 to surface-bound *CO and then to C_{2+} products, we posit that CO_2 first reduces to CO_{int} that accumulates to a concentrated reservoir near the catalyst surface before subsequent conversion to higher-order products (Fig. 3*B*).

Additionally, only a small fraction of the CO_{int} reservoir is converted per second to produce CO, C_2H_4, EtOH, and n-PrOH (Fig. 3*C*). The relative portion of the CO_{int} reservoir utilized per unit time (% s^{-1}) does not increase significantly and reaches only up to 1.05% per second as the potential is biased more negative. Instead, the distribution of products formed from the CO_{int} reservoir changes in favor of C_{2+} (Fig. 3*D*). Simultaneously, this shift in selectivity coincides with an increase of the CO_{int} density, roughly doubling from 78 to 147 molecules per Cu_{surf} (Fig. 3*D*). These observations suggest that

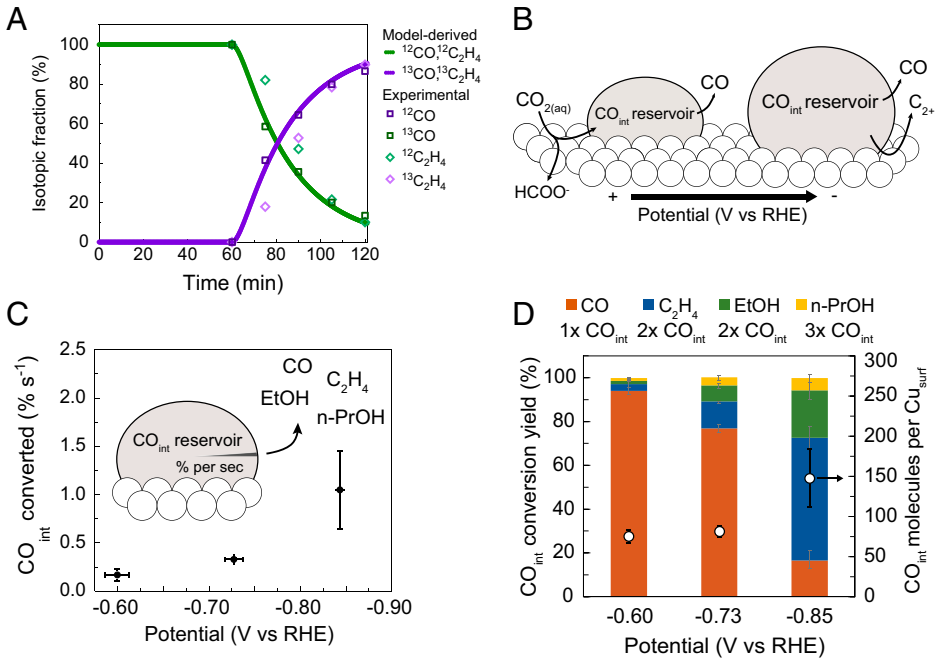

Fig. 3. Utilization of the CO_{int} reservoir on the Cu NP ensemble. (*A*) Comparison of the model-derived and experimental time-dependent change in the isotopic composition of CO and C_2H_4 over the course of OSRI at −0.85 V vs. RHE. $^{12}C_2H_4$ and $^{13}C_2H_4$ refer to the ^{12}C and ^{13}C fraction of all of C_2H_4 isotopologues ($^{12}CH_2$-$^{12}CH_2$, $^{12}CH_2$-$^{13}CH_2$, and $^{13}CH_2$-$^{13}CH_2$), respectively. (*B*) Schematic describing the formation and potential dependent utilization of the CO_{int} reservoir during CO_2RR. (*C*) The fraction of the CO_{int} reservoir converted per second to generate CO_{int}-derived products (sum of CO_{int} consumed per second for all CO_{int}-derived products/total of CO_{int} in the reservoir) as a function of applied potential. The rate of CO_{int} consumption for each CO_{int}-derived product is derived from its partial density and the number of CO_{int} required. (*D*) CO_{int} conversion yield (the number of CO_{int} consumed for one product/all CO_{int} consumed) partitioned across different CO_{int}-derived products and the CO_{int} density as a function of applied potential. The number of CO_{int} converted to each product is labeled as n× CO_{int}, where n corresponds to the number of CO_{int} required for its formation (e.g., 2× CO_{int} for C_2H_4). Error bars are one SD of three independent measurements.

C_{2+}-formation correlates with a sizeable amount of CO_{int} per Cu_{surf} (∼100 CO_{int}/Cu_{surf}). Interestingly, we note that a CO_{int} reservoir conversion of 1.05% per second is equivalent to a conversion rate of ∼1 CO_{int} monolayer per second. This indicates that, unlike a monolayer of CO_{int}, a large CO_{int} reservoir can sustain the necessary conditions to attain a conversion rate at the scale of a monolayer of intermediates per second.

Previous works have commented on the importance of obtaining high CO surface coverage to facilitate C-C coupling (22, 25, 55). The OSRI results suggest that this configuration extends to a CO_{int} reservoir present near the catalyst surface that may act as the source for C_{2+} formation downstream. Hence, the former notion of the traditional *CO monolayer is replaced with a locally concentrated large population of CO molecules as intermediates. Furthermore, OSRI experimentally verifies the often-speculated idea of CO-rich environments on the surface of Cu catalysts during CO_2 electrolysis (24–27).

To verify that the CO_{int} reservoir is not unique to the Cu NP ensemble catalyst, the OSRI method was applied to an electropolished Cu foil, a well-known benchmark Cu catalyst for CO_2RR. The potential range selected to study the Cu foil was negatively shifted in comparison to the Cu NP ensemble to generate a similar product distribution (*SI Appendix*, Fig. S23 and Table S8). Cu foil exhibits a similar gap in the ^{12}C isotopic fraction between $HCOO^-$ and all CO_{int}-derived products (*SI Appendix*, Fig. S24). Unlike the Cu NP ensemble, Cu foil displays a high FE toward CH_4 that allows for its isotopic distribution to be more thoroughly analyzed. The ^{12}C fraction of CH_4 is consistent with all other CO_{int}-derived products that corroborates the importance of CO as an intermediate for CH_4 production during CO_2 electroreduction (15, 56). However, a collection of gases (i.e., CO, CH_4, and C_2H_4) was detected when trying to identify the contents of the reservoir experimentally as described in Fig. 1*C* (*SI Appendix*, Supplementary Text 10 and Fig. S25). The presence of products such as CH_4 together with CO concentrated near the surface is expected to result from the morphological features of the Cu surface promoting the retention of gases (57). Therefore, the model was used to fit the Cu foil data while taking into consideration the presence of gases beyond CO as part of a larger reservoir regulating product formation and release (*SI Appendix*, Supplementary Text 11 and Fig. S26). Ultimately, the model closely replicates the experimental data, thus confirming the existence of a CO_{int} reservoir on Cu foil during CO_2RR (*SI Appendix*, Fig. S27).

Interestingly, both catalysts appear to enable C-C coupling after reaching a sufficiently high density of CO_{int} per Cu_{surf}. Similar to the Cu NP ensemble, an analysis of the Cu foil indicates a transition from C_1 to C_{2+} formation at a CO_{int} density of ∼100 CO_{int} per Cu_{surf} (Fig. 4*A*). The Cu foil further resembles the Cu NP ensemble with a CO_{int}-to-C_{2+} conversion rate of ∼1 CO_{int} monolayer per second that is achieved after reaching ∼100 CO_{int} per Cu_{surf} (*SI Appendix*, Fig. S28). These results suggest that a high surface coverage restricted to a monolayer does not provide the amount of CO_{int} necessary for C_{2+} formation. This principle is also in line with a recent finding showing that even a Ag catalyst can improve its otherwise negligible selectivity toward C_{2+} products given a high enough CO pressure (58). Taking these data, a key consideration in the development of catalysts moving forward should be increasing the CO_{int} density at lower overpotentials. Accordingly, the Cu NP ensemble reaches an adequate CO_{int} density at an overpotential 100 mV lower than the foil (Fig. 4*B*).

In addition to producing a sufficiently concentrated CO_{int} reservoir, a catalyst's activity should also be determined by its innate

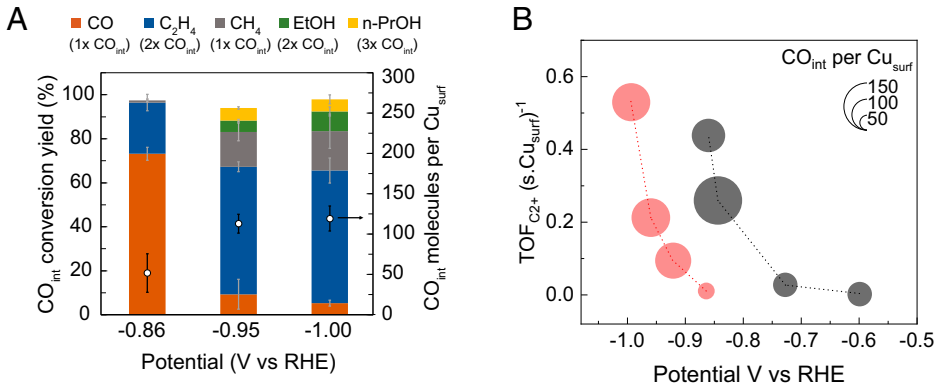

Fig. 4. Comparison between the Cu foil and the Cu NP ensemble. (*A*) CO_{int} conversion yield (CO_{int} consumed for each product/all CO_{int} consumed) partitioned across different CO_{int}-derived products and CO_{int} density measured as a function of applied potential on the Cu foil. The number of CO_{int} converted to each product is labeled as n× CO_{int}, where n corresponds to the number of CO_{int} required for its formation (e.g., 2× CO_{int} for C_2H_4). (*B*) C_{2+} turnover (dashed line) of the Cu foil and Cu NP ensemble with their CO_{int} density (by the size of the bubble) as a function of applied potential. Bubbles are plotted to scale with respect to their diameter. Error bars are one SD of three independent measurements.

ability to convert the CO_{int} reservoir to C_{2+}. So far, Cu-based electrocatalysts have been evaluated based on their C_{2+} FE and turnover at a fixed potential. However, such an analysis does not account for the availability of CO_{int}, which is critical; without the sufficient formation of CO_{int}, a catalyst is unlikely to form C_{2+} efficiently. Therefore, considering both the applied potential and availability of CO_{int} is necessary to accurately assess the intrinsic ability of a catalyst to form C_{2+} through the C-C coupling of C_1 intermediates. This is readily apparent in the comparison of C_{2+} turnover between the Cu NP ensemble and the foil around −0.85 V where the former displays a CO_{int} reservoir three times as large as the latter (Fig. 4*B*). This difference in the size of the CO_{int} reservoir brings into question whether the Cu foil may yield a C_{2+} turnover comparable to the NP ensemble provided there is enough CO_{int} allowed at a lower overpotential. However, we find this unlikely given the trend in the C_{2+} turnover frequency (TOF) of the Cu foil (Fig. 4*B*). Despite reaching a CO_{int} density of ∼100 CO_{int} per Cu_{surf}, its TOF does not rise steeply to reach comparable levels as the NP ensemble; a TOF of 0.1 C_{2+} per Cu_{surf} s^{-1} at −0.92 V is fourfold lower than the NP ensemble whose TOF is 0.4 C_{2+} per Cu_{surf} s^{-1} at only −0.86 V. Furthermore, under CO reduction (CORR) conditions with identical CO availability, we find that the NP ensemble exhibits higher TOF_{C2+} than the Cu foil as well (*SI Appendix*, Fig. S29). Hence, the formation of a concentrated CO_{int} reservoir is necessary but not sufficient for high C_{2+} turnover.

In addition, both catalysts reach noticeably higher levels of TOF_{C2+} during CO_2RR in comparison to CORR (*SI Appendix*, Fig. S29). This likely results from the formation of the reservoir during the electroreduction of CO_2, which sustains ∼100 CO molecules per Cu_{surf}. In contrast, within the 100-μm layer away from the catalyst surface, only 5 CO molecules per Cu_{surf} would be available under CORR. The concentrated CO microenvironment formed during CO_2RR overcomes the constraint of low CO solubility (1 mM in water at 1 atm, room temperature) that limits CORR activity in aqueous conditions. Therefore, instead of the concentration of CO_2, the size of the CO_{int} reservoir is a more accurate representation of the reactants necessary to the formation of multicarbons. We suggest that such considerations are also important for CO_2 reduction in gas-diffusion electrode systems; recent works have reported the importance of optimizing both the CO_2 and CO availability to maximize C-C coupling (55, 59, 60).

The results from the OSRI method suggest that both the contribution of CO_{int} availability and intrinsic C-C coupling ability are necessary to a catalyst's CO_2-to-C_{2+} activity. Concretely, a good catalyst must possess the ability to form a large CO_{int} reservoir at low overpotentials as well as exhibit high intrinsic activity for the coupling of CO_{int}. The Cu foil's moderate C_{2+} intrinsic activity is ascribed not only to its low intrinsic C-C coupling capacity but also to the high overpotential required to form a large enough CO_{int} reservoir. Therefore, maximizing CO_{int} availability at low overpotentials emerges as an additional parameter in future catalyst design, in addition to the necessary structural traits that favor C-C coupling (39, 61, 62). Namely, CO_{int} availability can be enhanced through improved retention of CO upon its formation. A few approaches along this line have been considered, such as modifying surface morphologies of electrodes to impact product release or functionalizing the catalyst with surface additives that promote gas affinity through increased hydrophobicity (28, 63–65). Beyond catalyst design implications, these results indicate that further investigations to determine the intrinsic C-C coupling of Cu-based catalysts under controlled (micro)environments are needed.

In summary, we present OSRI, a unique method that probes the microenvironment surrounding Cu surfaces during CO_2RR. It has led to the discovery of a concentrated reservoir of CO molecules near catalyst surfaces that is necessary for efficient C-C coupling. Instead of CO_2, this reservoir is identified as a more accurate representation of the reactants determining the rate of multicarbon formation during CO_2RR. Through these findings, the importance of the microenvironment formed during the reaction is better distinguished from the intrinsic activity of the catalyst surface. Furthermore, OSRI is a promising method to investigate the effects of the microenvironment in other catalytic reactions similar to CO_2RR. Specifically, the significance of intermediates residing near the surface during multistep electrocatalytic reactions can be gauged, thus guiding future improvements in catalyst selectivity and activity.

Materials and Methods

NP Synthesis and Electrode Fabrication. The 7-nm Cu NPs were synthesized as previously reported (39). NP concentrations by mass of Cu were measured by inductively coupled plasma optical emission spectroscopy (Perkin-Elmer Optima 7000 DV), after which 68.9 μg of Cu was deposited on a 1-cm^2 area of carbon paper (Sigracet 29AA, Fuel Cell Store) to make working electrodes.

Cu foil (0.1 mm thick, Puratronic, 99.999%) was electropolished before utilization in 85% phosphoric acid at 3 V against a counter electrode for 1 min. Once treated, the Cu foil was thoroughly rinsed with deionized water and dried with N_2 gas. The electrode of a 4-cm^2 geometric surface area was placed inside an electrochemical cell for further testing.

OSRI. All electrochemical measurements were carried in a custom-made H-cell consisting of two main compartments separated by a Selemion AMV anion exchange membrane (AEM). Ag/AgCl (WPI, 3 M KCl) was used as a reference electrode, and a platinum wire was used as a counter electrode. A total of 0.1 M $KHCO_3$ electrolyte was prepared by purging a 0.05 M K_2CO_3 (99.997% trace metal basis) solution with $CO_{2(g)}$ overnight. Both the working and counter chamber were filled with 15 mL of the electrolyte, and vigorous stirring was maintained in the working chamber. The input stream of $CO_{2(g)}$ was humidified by being bubbled through distilled water before being introduced into the cell. Before each measurement, the 15-mL catholyte was purged with 20 sccm $^{12}CO_{2(g)}$ for 15 to 20 min until saturated. Then, $^{12}CO_{2(g)}$ was purged while applying a cathodic bias for 60 min and subsequently switched to $^{13}CO_{2(g)}$ (^{13}C dioxide, 99 atom % ^{13}C, 99.93 atom % ^{16}O) while maintaining the same potential for another 60 min. Depending on the operating conditions, the flow rate was adjusted to 20, 10, or 5 sccm. For instance, low flow rates were used for conditions that exhibit low current densities (e.g., at more positive potentials). This ensured higher concentrations of gas products to be measured in real time using the gas chromatograph. All electrode potentials measured against the 3 M KCl Ag/AgCl reference were converted to the RHE scale using E (vs. RHE) = E (vs. Ag/AgCl) + 0.210 V + 0.0591 × pH. For all electrochemical experiments, 84% of ohmic loss was compensated by the potentiostat (Biologic) in real time and the remaining 16% was manually postcorrected.

The concentration of gases produced throughout OSRI were measured regardless of their isotopic identity using a gas chromatograph (SRI GC) connected at the outlet of the cell. The gas chromatograph is equipped with a molecular sieve 13× (1/8″ × 6′) and hayesep D (1/8″ × 6′) column with Ar flowing as a carrier gas. A sample for GC was collected at 20-min intervals, and the separated gas products were analyzed by a thermal conductivity detector (TCD) for H_2 and a flame ionization detector (FID) for CO and hydrocarbons. Quantification of the products was performed with conversion factors derived from the standard calibration gases, and the concentration of gas measured was further converted to partial current density.

Upon substitution of the reactant isotope from $^{12}CO_{2(g)}$ to $^{13}CO_{2(g)}$, all produced gases were collected to determine their isotopic composition. A 2-L Supel-Inert multilayer foil gas bag (gas bag #1) was connected to the exhaust of the SRI GC sampling loop at the same time as the onstream substitution at 60 min. After another 60 min of electrolysis while purging $^{13}CO_{2(g)}$, the application of bias was terminated, and the gas stream was substituted with Ar. Gas bag #1 was simultaneously sealed and substituted for a second bag (gas bag #2) to collect any leftover gases still present inside the cell to determine the size and composition of the CO_{int} reservoir (see *Materials and Methods* section *Determining the Size and Isotopic Composition of the COint Reservoir*).

The isotopic composition of gas products in gas bag #1 was determined by GC-MS using an AutoSpec Premier mass spectrometer (Waters), equipped with an Agilent 7890A gas chromatograph, and an electron impact ion source. The collected gases were sampled and manually injected using a gas-tight 1-mL syringe (Agilent PN 5190-1531). They were pushed through a Supelco, Carboxen- 1010 PLOT column with He as a carrier gas to separate CO, CH_4, and C_2H_4 from N_2, O_2 and CO_2 (*SI Appendix*, Fig. S1). The mass spectrograms were analyzed to extract the isotopic composition of all CO_2RR gas products as described in *SI Appendix*, Supplementary Text 1.

Meanwhile, the liquid products accumulated during OSRI were analyzed by quantitative NMR (Bruker AV-600) using dimethyl sulfoxide as an internal standard. The solvent presaturation technique was implemented to suppress the water peak. The collection of all liquid products was ensured by analyzing the catholyte and the AEM. The latter was soaked in 15-mL blank electrolyte overnight to ensure all trapped products would diffuse back into the liquid (*SI Appendix*, Supplementary Text 2). A further isotope analysis was carried on the liquid products combining ^1H with ^{13}C NMR on the same instrument. ^{13}C NMR required a long acquisition time (>9 h) to accumulate enough signal due to low concentrations. The isotopic composition of liquid products (e.g., $HCOO^-$, EtOH) was determined by decoupling the signals from their multiple isotopologues as described in *SI Appendix*, Supplementary Text 3.

FEs were calculated from the amount of charge passed to produce each product divided by the total charge passed at a specific time (gas) or during the overall run (liquid).

Determining the Size and Isotopic Composition of the CO_{int} Reservoir. After the second hour of electrolysis while purging $^{13}CO_{2(g)}$, the bias was terminated and all CO present in the cell was purged out with Ar for 60 min and collected in gas bag #2. Ar purge of 60 min ensured that there were no remaining gases in the working electrode chamber. Depending on the flow rate employed for each experiment, ranging from 5 to 20 sccm, gas bag #2 was filled with a total gas volume of 300 to 1,200 mL, respectively. The low CO concentration collected in gas bag #2 was measured after injecting the bag content into another gas chromatograph (Agilent 7890B GC) setup for manual injection. This gas chromatograph is equipped with a molecular sieve SA (60/80″ × 6′), hayesep Q (80/100″ × 6′), and hayesep Q (80/100″ x 1.5′) column with Ar flowing as a carrier gas. The same detectors (i.e., FID and TCD) listed for the SRI GC are used. Using the measured CO concentration, the total amount of CO molecules was calculated considering the total volume of gas collected. Gas bag #2 contained CO collected from the headspace, dissolved in the bulk electrolyte, and locally concentrated near the catalyst surface (i.e., CO_{int} reservoir), which were all present upon stopping bias. CO present in the cell headspace was determined from the concentration of CO measured at steady state during electrolysis (SRI GC) and the headspace volume of 30 mL. Furthermore, Henry's law was applied to obtain the number of dissolved CO in equilibrium with that headspace. The size of the CO_{int} reservoir was estimated by subtracting both values from the total amount of CO collected in gas bag #2. The isotopic composition of the CO_{int} reservoir was determined following the GC-MS procedure (described for gas bag #1) applied to gas bag #2. The composition of the CO_{int} reservoir is assumed to be identical to the headspace and dissolved CO. The same method of quantification was employed at more negative potentials.

ECSA and Cu Surface Atom Determination. Lead underpotential deposition (Pb UPD) was conducted immediately postelectrolysis in a solution of 0.1 M $NaClO_4$, 10 mM $HClO_4$, and 3 mM $Pb(II)(ClO_4)_2$. Cyclic voltammetry in the Pb underpotential region was conducted at 10 mV/s six times, for which the cycles were confirmed consistent, and the fifth scan was reported. The potentials are referenced against a 1.0 M KCl Ag/AgCl electrode.

The number of Cu surface atoms was then determined using the assumption that each of the low index facets (100), (110), and (111) are equally likely to be present on the surface. We used the relationship between the number of Cu atoms and surface area for each facet as established in the work of Giri and Sakar to determine the number of surface Cu atoms from the measured Cu surface area by Pb UPD (66).

$$\text{Planar density of Cu(100)plane} = 15.3065 \times 10^{14}\ \frac{\text{atoms}}{\text{cm}^2}$$

$$\text{Planar density of Cu(110)plane} = 10.8371 \times 10^{14}\ \frac{\text{atoms}}{\text{cm}^2}$$

$$\text{Planar density of Cu(111)plane} = 17.7556 \times 10^{14}\ \frac{\text{atoms}}{\text{cm}^2}$$

COMSOL Multiphysics Simulation. The change in isotopic composition taking place during the purge of $^{13}CO_2$ gas into a $^{12}CO_2$ equilibrated electrolyte was simulated using COMSOL Multiphysics. The transport of species present was calculated for the bulk volume of the well-mixed electrolyte. The Bubbly Flow, Laminar Flow module was used to solve for the velocity and mass transfer of CO_2 bubbles into the liquid electrolyte. Assuming only a small volume fraction is occupied by the bubbles, the Navier–Stokes equations were used only to solve for the flow of the liquid phase while the velocity of the bubbles was determined by a slip model. The gas mass flux was set to replicate the experimental flow rate employed during OSRI (e.g., 5 sccm) with a bubble size of 0.4 cm. The number of bubbles per unit volume is tracked over time within the electrolyte to calculate the total interfacial area a (m^2). Mass transport m_{gl} ($kg \cdot s^{-1}$) taking place at this interface was calculated using two-film theory:

$$m_{gl} = k(c^* - c)Ma, \quad c^* = \frac{p + p_{ref}}{H}$$

where k (m.s^{-1}) corresponds to the mass transfer coefficient, c (mol.m^{-3}) corresponds to the concentration of the gas dissolved in solution, M (kg.mol^{-1}) corresponds to the gas molecular weight, p (Pa) corresponds to the gas pressure, and H is Henry's constant (Pa.m^3.mol^{-1}). Upon dissolution, the further equilibration of CO_2 at pH <7 is described by the following equations:

$$CO_2 + H_2O \rightleftarrows HCO_3^- + H^+ \quad pKa_1 = 6.37$$

$$HCO_3^- \rightleftarrows CO_3^{2-} + H^+ \quad pKa_2 = 10.25$$

Water self-ionization equilibrium is also included:

$$H_2O \rightleftarrows OH^- + H^+ \quad pK_w = 14$$

Using their respective equilibrium constants, the concentrations of all species present in the electrolyte were solved for, using the Transport of Dilute Species module. Dissolved $CO_{2(aq)}$, bicarbonate anions (HCO_3^-), carbonate anions (CO_3^{2-}), hydroxide anions (OH^-), protons (H^+), and potassium cations (K^+) were all accounted for during the time-dependent study. All ^{12}C and ^{13}C equivalents were considered for all carbon-containing species. The initial concentration of all species was established assuming the 0.1 M $KH^{12}CO_3$ electrolyte is equilibrated under a $^{12}CO_2$-saturated atmosphere and respects the condition of electroneutrality:

$$\sum_i z_i c_i = 0$$

Following the introduction of $^{13}CO_{2(g)}$, the transport of all solvated species was set to respect mass conservation such as:

$$\frac{\partial c_i}{\partial t} + \nabla \cdot \mathbf{J} + \mathbf{u} \cdot c_i = R_i, \quad \mathbf{J}_i = -D_i \nabla c_i - z_i u_{m,i} F c_i \nabla V$$

where c_i corresponds to the concentration of the species, D_i corresponds to their diffusion coefficient, R_i corresponds to their reaction rate expression, u corresponds to the mass average velocity vector, J_i corresponds to the mass flux diffusive flux vector, z_i corresponds to the charge number of the ionic species, $u_{m,i}$ corresponds to their ionic mobility, F is Faraday's constant, and V corresponds to the electric potential. The velocity u describes the convective transport that results from the magnetic stirring in the cell as well as the bubbly flow solved in the previous module. All constants utilized for the simulation are summarized in *SI Appendix*, Table S6.

OSRI Kinetic Model. Molecular mass flow taking place during OSRI was modeled to reproduce the composition of isotopes observed in the products. The model was built based on the kinetic relationship between supplied $CO_{2(g)}$, available $CO_{2(aq)}$, a CO_{int} reservoir, and all CO_2RR products. Once determined mathematically as described in the *SI Appendix*, Supplementary Text 6, the model was run using MATLAB.

CORR Measurements. CORR experiments were conducted in a similar three-electrode electrochemical H-cell constructed from polytetrafluoroethylene, using 0.1 M KOH (Sigma, 99.99%) as electrolyte. CO (99.99%, Praxair) was purged through the electrolyte for at least 30 min before electrolysis and maintained at 15 sccm throughout electrolysis. Hg/HgO 1 M NaOH (0.13 V vs. standard hydrogen electrode [SHE]) reference electrode and Neosepta AHA membrane were used for their tolerance to the alkaline electrolyte. Electrolysis was conducted for 30 min to 1 h before gas and liquid samples were collected. All gas and liquid products were analyzed using the same procedure described above for GC and NMR measurements, respectively.

Data Availability. All study data are included in the article and/or *SI Appendix*.

ACKNOWLEDGMENTS. This work was supported by the Director, Office of Science, Office of Basic Energy Sciences, Chemical Sciences, Geosciences, & Biosciences Division, of the US Department of Energy under Contract DE-AC02-05CH11231, FWP CH030201 (Catalysis Research Program). Inductively coupled plasma-optical emission spectrometry was supported by the Microanalytical Facility, College of Chemistry, UC Berkeley. We thank College of Chemistry;s NMR facility for resources provided and the staff for their assistance. Instruments in the College of Chemistry NMR facility are supported in part by NIH S10OD024998. We thank Z. Zhou at the QB3 Chemistry Mass Spectrometry Facility for her assistance with GC-MS measurements. Computational work using COMSOL Multiphysics was done at the Molecular Graphics and Computation Facility, UC Berkeley, which is supported by NIH S10OD023532. D.K. and S.Y. acknowledge support from the Samsung Scholarship.

1. P. De Luna *et al.*, What would it take for renewably powered electrosynthesis to displace petrochemical processes? *Science* **364**, eaav3506 (2019).
2. D. E. Blanco, M. A. Modestino, Organic electrosynthesis for sustainable chemical manufacturing. *Trends Chem.* **1**, 8–10 (2019).
3. J. Na *et al.*, General technoeconomic analysis for electrochemical coproduction coupling carbon dioxide reduction with organic oxidation. *Nat. Commun.* **10**, 5193 (2019).
4. D. Kim *et al.*, Selective CO_2 electrocatalysis at the pseudocapacitive nanoparticle/ordered-ligand interlayer. *Nat. Energy* **5**, 1032–1042 (2020).
5. N. Ramaswamy *et al.*, Hydrogen oxidation reaction in alkaline media: Relationship between electrocatalysis and electrochemical double-layer structure. *Nano Energy* **41**, 765–771 (2017).
6. W. Chen *et al.*, Probing complex eletrocatalytic reactions using electrochemical infrared spectroscopy. *Curr. Opin. Electrochem.* **14**, 113–123 (2019).
7. F. Zaera, Probing liquid/solid interfaces at the molecular level. *Chem. Rev.* **112**, 2920–2986 (2012).
8. Y. Zhu, J. Wang, H. Chu, Y.-C. Chu, H. M. Chen, In situ/operando studies for designing next-generation electrocatalysts. *ACS Energy Lett.* **5**, 1281–1291 (2020).
9. L. Lancaster, W. Abdallah, S. Banta, I. Wheeldon, Engineering enzyme microenvironments for enhanced biocatalysis. *Chem. Soc. Rev.* **47**, 5177–5186 (2018).
10. H. M. Colquhoun, J. F. Stoddart, D. J. Williams, Second-sphere coordination–A novel röle for molecular receptors. *Angew. Chem. Int. Ed. Engl.* **25**, 487–507 (1986).
11. L. V. Hale, N. K. Szymczak, Hydrogen transfer catalysis beyond the primary coordination sphere. *ACS Catal.* **8**, 6446–6461 (2018).
12. Y. Cao, X. Li, J. Ge, Enzyme catalyst engineering toward the integration of biocatalysis and chemocatalysis. *Trends Biotechnol.* **39**, 1173–1183 (2021).
13. M. Vázquez-González, C. Wang, I. Willner, Biocatalytic cascades operating on macromolecular scaffolds and in confined environments. *Nat. Catal.* **3**, 256–273 (2020).
14. Y. Zhang, Q. Wang, H. Hess, Increasing enzyme cascade throughput by pH-engineering the microenvironment of individual enzymes. *ACS Catal.* **7**, 2047–2051 (2017).
15. S. Nitopi *et al.*, Progress and perspectives of electrochemical CO_2 reduction on copper in aqueous electrolyte. *Chem. Rev.* **119**, 7610–7672 (2019).
16. Y. Kim *et al.*, Time-resolved observation of C–C coupling intermediates on Cu electrodes for selective electrochemical CO_2 reduction. *Energy Environ. Sci.* **13**, 4301–4311 (2020).
17. E. Pérez-Gallent, M. C. Figueiredo, F. Calle-Vallejo, M. T. Koper, Spectroscopic observation of a hydrogenated CO dimer intermediate during CO reduction on Cu (100) electrodes. *Angew. Chem. Int. Ed. Engl.* **56**, 3621–3624 (2017).
18. A. Wuttig, J. Ryu, Y. Surendranath, Electrolyte competition controls surface binding of CO intermediates to CO_2 reduction catalysts. *J. Phys. Chem. C* **125**, 17042–17050 (2021).
19. F. Li *et al.*, Molecular tuning of CO_2-to-ethylene conversion. *Nature* **577**, 509–513 (2020).
20. T.-C. Chou *et al.*, Controlling the oxidation state of the Cu electrode and reaction intermediates for electrochemical CO_2 reduction to ethylene. *J. Am. Chem. Soc.* **142**, 2857–2867 (2020).
21. C. M. Gunathunge, V. J. Ovalle, Y. Li, M. J. Janik, M. M. Waegele, Existence of an electrochemically inert CO population on Cu electrodes in alkaline pH. *ACS Catal.* **8**, 7507–7516 (2018).
22. Y. Huang, A. D. Handoko, P. Hirunsit, B. S. Yeo, Electrochemical reduction of CO_2 using copper single-crystal surfaces: Effects of CO* coverage on the selective formation of ethylene. *ACS Catal.* **7**, 1749–1756 (2017).
23. R. B. Sandberg, J. H. Montoya, K. Chan, J. K. Nørskov, CO-CO coupling on Cu facets: Coverage, strain and field effects. *Surf. Sci.* **654**, 56–62 (2016).
24. A. Wuttig *et al.*, Tracking a common surface-bound intermediate during CO_2-to-fuels catalysis. *ACS Cent. Sci.* **2**, 522–528 (2016).
25. E. L. Clark, A. T. Bell, Direct observation of the local reaction environment during the electrochemical reduction of CO_2. *J. Am. Chem. Soc.* **140**, 7012–7020 (2018).
26. S. Jiang, K. Klingan, C. Pasquini, H. Dau, New aspects of operando Raman spectroscopy applied to electrochemical CO_2 reduction on Cu foams. *J. Chem. Phys.* **150**, 041718 (2019).
27. K. Klingan *et al.*, Reactivity determinants in electrodeposited Cu foams for electrochemical CO_2 reduction. *ChemSusChem* **11**, 3449–3459 (2018).
28. D. Wakerley *et al.*, Bio-inspired hydrophobicity promotes CO_2 reduction on a Cu surface. *Nat. Mater.* **18**, 1222–1227 (2019).
29. O. Baturina *et al.*, Effect of nanostructured carbon support on copper electrocatalytic activity toward CO_2 electroreduction to hydrocarbon fuels. *Catal. Today* **288**, 2–10 (2017).
30. P. B. O'Mara *et al.*, Cascade reactions in nanozymes: Spatially separated active sites inside Ag-Core–Porous-Cu-shell nanoparticles for multistep carbon dioxide reduction to higher organic molecules. *J. Am. Chem. Soc.* **141**, 14093–14097 (2019).
31. M. Dunwell *et al.*, Examination of near-electrode concentration gradients and kinetic impacts on the electrochemical reduction of CO_2 using surface-enhanced infrared spectroscopy. *ACS Catal.* **8**, 3999–4008 (2018).
32. J. Heyes, M. Dunwell, B. Xu, CO_2 reduction on Cu at low overpotentials with surface-enhanced in situ spectroscopy. *J. Phys. Chem. C* **120**, 17334–17341 (2016).
33. N. Heidary, K. H. Ly, N. Kornienko, Probing CO_2 conversion chemistry on nanostructured surfaces with operando vibrational spectroscopy. *Nano Lett.* **19**, 4817–4826 (2019).
34. A. D. Handoko, F. Wei, B. S. Yeo, Z. W. Seh, Understanding heterogeneous electrocatalytic carbon dioxide reduction through operando techniques. *Nat. Catal.* **1**, 922–934 (2018).
35. M. Osawa, K.-I. Ataka, K. Yoshii, Y. Nishikawa, Surface-enhanced infrared spectroscopy: The origin of the absorption enhancement and band selection rule in the infrared spectra of molecules adsorbed on fine metal particles. *Appl. Spectrosc.* **47**, 1497–1502 (1993).
36. G. C. Schatz, Theoretical studies of surface enhanced Raman scattering. *Acc. Chem. Res.* **17**, 370–376 (1984).
37. P. L. Stiles, J. A. Dieringer, N. C. Shah, R. P. Van Duyne, Surface-enhanced Raman spectroscopy. *Annu. Rev. Anal. Chem. (Palo Alto, Calif.)* **1**, 601–626 (2008).
38. R. Kas *et al.*, In-situ infrared spectroscopy applied to the study of the electrocatalytic reduction of CO_2: Theory, practice and challenges. *ChemPhysChem* **20**, 2904–2925 (2019).

39. Y. Li *et al.*, Electrochemically scrambled nanocrystals are catalytically active for CO_2-to-multicarbons. *Proc. Natl. Acad. Sci. U.S.A.* **117**, 9194–9201 (2020).
40. A. A. Peterson, F. Abild-Pedersen, F. Studt, J. Rossmeisl, J. K. Nørskov, How copper catalyzes the electroreduction of carbon dioxide into hydrocarbon fuels. *Energy Environ. Sci.* **3**, 1311–1315 (2010).
41. Y. Hori, "Electrochemical CO_2 Reduction on Metal Electrodes" in *Modern Aspects of Electrochemistry*, C. G. Vayenas, R. E. White, M. E. Gamboa-Aldeco, Eds. (Springer, 2008), pp. 89–189.
42. I. V. Chernyshova, P. Somasundaran, S. Ponnurangam, On the origin of the elusive first intermediate of CO_2 electroreduction. *Proc. Natl. Acad. Sci. U.S.A.* **115**, E9261–E9270 (2018).
43. H. A. Hansen, J. B. Varley, A. A. Peterson, J. K. Nørskov, Understanding trends in the electrocatalytic activity of metals and enzymes for CO_2 reduction to CO. *J. Phys. Chem. Lett.* **4**, 388–392 (2013).
44. M. Gattrell, N. Gupta, A. Co, A review of the aqueous electrochemical reduction of CO_2 to hydrocarbons at copper. *J. Electroanal. Chem. (Lausanne)* **594**, 1–19 (2006).
45. Gurudayal *et al.*, Sequential cascade electrocatalytic conversion of carbon dioxide to C–C coupled products. *ACS Appl. Energy Mater.* **2**, 4551–4559 (2019).
46. Y. Lum, J. W. Ager, Sequential catalysis controls selectivity in electrochemical CO_2 reduction on Cu. *Energy Environ. Sci.* **11**, 2935–2944 (2018).
47. J. Gao *et al.*, Selective C-C coupling in carbon dioxide electroreduction via efficient spillover of intermediates as supported by operando Raman spectroscopy. *J. Am. Chem. Soc.* **141**, 18704–18714 (2019).
48. C. G. Morales-Guio *et al.*, Improved CO_2 reduction activity towards C_{2+} alcohols on a tandem gold on copper electrocatalyst. *Nat. Catal.* **1**, 764–771 (2018).
49. T. H. Phan *et al.*, Emergence of potential-controlled Cu-nanocuboids and graphene-covered Cu-nanocuboids under *Operando* CO_2 electroreduction. *Nano Lett.* **21**, 2059–2065 (2021).
50. H. Vogt, On the supersaturation of gas in the concentration boundary layer of gas evolving electrodes. *Electrochim. Acta* **25**, 527–531 (1980).
51. S. R. German *et al.*, Electrochemistry of single nanobubbles. Estimating the critical size of bubble-forming nuclei for gas-evolving electrode reactions. *Faraday Discuss.* **193**, 223–240 (2016).
52. Q. Chen, H. S. Wiedenroth, S. R. German, H. S. White, Electrochemical nucleation of stable N_2 nanobubbles at Pt nanoelectrodes. *J. Am. Chem. Soc.* **137**, 12064–12069 (2015).
53. H. Ren, S. R. German, M. A. Edwards, Q. Chen, H. S. White, Electrochemical generation of individual O_2 nanobubbles via H_2O_2 oxidation. *J. Phys. Chem. Lett.* **8**, 2450–2454 (2017).
54. X. Zhao, H. Ren, L. Luo, Gas bubbles in electrochemical gas evolution reactions. *Langmuir* **35**, 5392–5408 (2019).
55. Y. C. Tan, K. B. Lee, H. Song, J. Oh, Modulating local CO_2 concentration as a general strategy for enhancing C— C coupling in CO_2 electroreduction. *Joule* **4**, 1104–1120 (2020).
56. X. Zhou *et al.*, Stabilizing Cu^{2+} ions by solid solutions to promote CO_2 electroreduction to methane. *J. Am. Chem. Soc.* **144**, 2079–2084 (2022).
57. W. Xu, Z. Lu, X. Sun, L. Jiang, X. Duan, Superwetting electrodes for gas-involving electrocatalysis. *Acc. Chem. Res.* **51**, 1590–1598 (2018).
58. S. J. Raaijman, M. P. Schellekens, P. J. Corbett, M. T. M. Koper, C. O. High-Pressure, High-pressure CO electroreduction at silver produces ethanol and propanol. *Angew. Chem. Int. Ed. Engl.* **60**, 21732–21736 (2021).
59. X. Wang *et al.*, Mechanistic reaction pathways of enhanced ethylene yields during electroreduction of CO_2-CO co-feeds on Cu and Cu-tandem electrocatalysts. *Nat. Nanotechnol.* **14**, 1063–1070 (2019).
60. Z. Xing, L. Hu, D. S. Ripatti, X. Hu, X. Feng, Enhancing carbon dioxide gas-diffusion electrolysis by creating a hydrophobic catalyst microenvironment. *Nat. Commun.* **12**, 136 (2021).
61. H. Jung *et al.*, Electrochemical fragmentation of Cu_2O nanoparticles enhancing selective C–C coupling from CO_2 reduction reaction. *J. Am. Chem. Soc.* **141**, 4624–4633 (2019).
62. A. Loiudice *et al.*, Tailoring copper nanocrystals towards C_2 products in electrochemical CO_2 reduction. *Angew. Chem. Int. Ed. Engl.* **55**, 5789–5792 (2016).
63. T. Burdyny *et al.*, Nanomorphology-enhanced gas-evolution intensifies CO_2 reduction electrochemistry. *ACS Sustain. Chem.& Eng.* **5**, 4031–4040 (2017).
64. S. Khan, J. Hwang, Y.-S. Horn, K. K. Varanasi, Catalyst-proximal plastrons enhance activity and selectivity of carbon dioxide electroreduction. *Cell Rep. Phys. Sci.* **2**, 100318 (2021).
65. P. Yue *et al.*, Triple-phase electrocatalysis for the enhanced CO_2 reduction to HCOOH on a hydrophobic surface. *Chem. Eng. J.* **405**, 126975 (2021).
66. S. D. Giri, A. Sarkar, Estimating surface area of copper powder: A comparison between electrochemical, microscopy and laser diffraction methods. *Adv. Powder Technol.* **29**, 3520–3526 (2018).